Materials & Design 233 (2023) 112170

Contents lists available at ScienceDirect

Materials & Design

journal homepage: www.elsevier.com/locate/matdes

Post-fabrication tuning of origami-inspired mechanical metamaterials based on Tachi-Miura Polyhedron

Koshiro Yamaguchi [a], Yasuhiro Miyazawa [a], Hiromi Yasuda [b], Yuyang Song [c], Shinnosuke Shimokawa [c], Umesh Gandhi [c], Jinkyu Yang [a,d,*]

[a] William E. Boeing Department of Aeronautics and Astronautics, University of Washington, Seattle, WA 98195-2400, USA
[b] Aviation Technology Directorate, Japan Aerospace Exploration Agency, Mitaka, Tokyo 1810015, Japan
[c] Toyota Research Institute North America, 1555 Woodridge Ave, Ann Arbor, MI 48105, USA
[d] Department of Mechanical Engineering, Seoul National University, 1 Gwanak-ro, Gwanak-gu, Seoul 08826, Republic of Korea

ARTICLE INFO

Keywords:
Mechanical metamaterials
Reconfigurable systems
Origami engineering

ABSTRACT

We investigate the reconfigurability and tunability of the tessellation of Tachi-Miura Polyhedron (TMP), an origami-based cellular structure composed of bellows-like unit cells. Lattice-based three-dimensional mechanical metamaterials have recently received significant scientific interest due to their superior and unique mechanical performance compared to conventional materials. However, it is often challenging to achieve tunability and reconfigurability from these metamaterials, since their geometry and functionality tend to be predetermined in the design and fabrication stage. Here, we utilize TMP's highly versatile phase-transforming and tessellating capabilities to design reconfigurable metamaterial architecture with tunable mechanical properties. The theoretical analyses and experiments with heat processing discover the wide range of the in-situ tunability of the metamaterial – specifically orders of magnitude change in effective density, Young's modulus, and Poisson's ratio – after its fabrication within the elastic deformation regime. We also witness a rather unique behavior of the inverse correlation between effective density and stiffness. This mechanical platform paves the way to design the metamaterial that can actively adapt to various external environments.

1. Introduction

Mechanical metamaterials offer unprecedented mechanical properties and rich functionalities due to the plentiful design freedom available within their architecture [1–3]. Among a variety of approaches to constructing metamaterials with such unique properties, lattice-based mechanical metamaterials are emerging concepts [4–6]. Their voluminous nature and extreme mechanical properties have the possibility to work as three-dimensional constructional elements of the mechanical system while achieving superior performance compared to conventional materials. Examples include metamaterial with negative elastic constant [4], labyrinthine acoustic metamaterials to slow down sound propagation [5], and 3D-printed lattices with both lightness and stiffness in an extreme range [6]. While their unique properties can be leveraged in multiple fields, such as mechanical, aerospace, and biomedical engineering, these metamaterials have challenges in terms of cost of manufacturing and post-fabrication tunability due to their complicated and unadjustable architecture.

To overcome these obstacles, various designs have been introduced in the realm of flexible mechanical metamaterials [7] and origami-inspired structures [8]. Examples include programmable flexible mechanical metamaterials with adjustable Poisson's ratio, Young's modulus, or negative thermal expansion coefficient [9–11], origami tessellation by Resch-pattern [12,13], reprogrammable origami mechanical metamaterials [14], stiff yet reconfigurable origami tubes [15], shape-changing prismatic architected materials [16], and multistable origami at metre scale [17]. However, these studies also present several limitations. First, certain designs are not suitable for constructing three-dimensional, space-filling, and voluminous metamaterials due to their planar configuration [10,12–14]. Second, mechanisms reliant on surface-contact locking, non-rigid panel assumptions, or discrete morphing stages make it difficult to achieve an accurate prediction and continuous tuning of mechanical properties [9,13–17]. To tackle these issues, we aim to develop an engineering platform with the following features: (i) extensive and continuous design space, and post-fabrication tunability for three key mechanical properties — effective density,

* Corresponding author at: Department of Mechanical Engineering, Seoul National University, 1 Gwanak-ro, Gwanak-gu, Seoul 08826, Republic of Korea.
E-mail address: jkyang11@snu.ac.kr (J. Yang).

https://doi.org/10.1016/j.matdes.2023.112170
Received 10 May 2023; Received in revised form 12 July 2023; Accepted 13 July 2023
Available online 25 July 2023

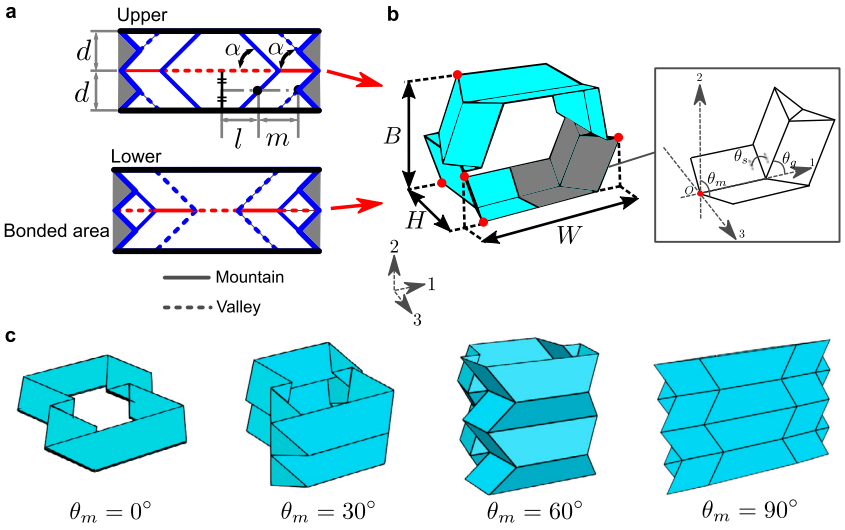

Fig. 1. A unit cell of Tachi-Miura Polyhedron. **a**, the definition of crease patterns and geometrical parameters of two flat-foldable sheets composing the TMP. Red and blue lines represent the main (horizontal) and sub (inclined) crease lines, respectively. Grey-colored areas represent the bonding region to construct a unit cell. **b**, a unit cell of Tachi-Miura Polyhedron composed of two origami sheets. Dimensions B, W, and H correspond to the width, breadth, and height of the structure, respectively. The inset in **b** is a Miura-folding unit cell that corresponds to the gray area in **b**. **c**, folding process of a TMP unit cell. Each picture corresponds to folding angles $\theta_m = 0°$, $\theta_m = 30°$, $\theta_m = 60°$, and $\theta_m = 90°$, from left to right.

Poisson's ratio, and Young's modulus, (ii) the ability to easily predict these properties through analytical methods, and (iii) an efficient and straightforward fabrication of multi-cell 3D structures by simply joining layers, eliminating the need for cell-by-cell assembly.

We introduce the Tachi-Miura Polyhedron (TMP) as a promising platform to achieve tunability in three-dimensional mechanical metamaterials after the fabrication phase. TMP is an origami-based mechanical metamaterial characterized by bellows-like 3D unit cells originating from 2D Miura-folding sheets, and TMP can be tessellated to provide load-bearing capacity [18–21]. By employing rigid panels and torsional springs along the crease lines in TMP unit cells [22], the analysis of mechanical properties and design space within the elastic deformation regime, where mechanical properties are tunable, is greatly simplified. Furthermore, the design space can be broadened due to the adjustable Poisson's ratio spanning both positive and negative ranges [22–24]. Our analysis is substantiated through experiments on a prototype fabricated using an efficient method inspired by honeycomb structures. This yields approximately 60-time and 10-time variations in Young's modulus and effective density, respectively. We also visualize the tunability of the TMP in an Ashby chart [25] and report unique features such as anisotropic positive/negative Poisson's ratios and an increase in stiffness correlated with a decrease in effective density. These features are represented in three-dimensional extended Ashby charts.

2. Methods and materials

2.1. Prototype fabrication

2.1.1. Construction of a TMP unit cell

A TMP unit cell is composed of two flat-foldable origami sheets, featuring four adjustable geometric design parameters (l, m, d, α) as illustrated in Fig. 1(a). By assigning appropriate folding directions (mountain or valley) to these origami sheets and combining them, a unit cell can be formed, as seen in Fig. 1(b). The dimensions of a unit cell, such as breadth, height, and width, can be defined and calculated in terms of the aforementioned geometrical parameters under the rigid foldability assumption [22]. Additionally, folding angles θ_m, θ_s, and θ_g as indicated in the Miura-ori subset (see the inset of Fig. 1(b)) can be established to describe the folding state (posture) of TMP. Owing to the nature of the origami sheet components, a TMP unit cell can exhibit two flat-folded states ($\theta_m = 0°$ and $\theta_m = 90°$) and a wide range of dimensional variations in a transient state, as demonstrated in Fig. 1(c). Detailed kinematic analysis of a TMP unit cell can be found in Supplementary Note A.

2.1.2. Strategies to construct a TMP tessellation

In this section, we explore approaches to manufacturing a prototype of a TMP tessellation. Prior research on TMP tessellation employs a cell-by-cell manufacturing technique, in which each fabricated unit cell is combined to form a tessellation [18], as depicted schematically in Fig. 2(a). This method has its own merits, such as the modular construction of the structure. However, it necessitates the production of multiple TMP unit cells and results in increased manufacturing time and redundant materials at the interfacial walls between the cells. Thus, to attain manufacturing efficiency, we adopt a method inspired by the fabrication process of honeycomb structures, where corrugated sheets are connected [26]. Previous work on honeycomb-inspired origami structures demonstrates its efficiency in terms of manufacturing [27,28]. In this study, we expand the concept of honeycomb-inspired origami structures for the efficient fabrication of TMP-based mechanical metamaterials.

To this end, it is preferable to fabricate large portions of the origami structure, corrugate, and assemble them collectively. Fig. 2(b) presents schematic illustrations of a layer-by-layer manufacturing process. In Fig. 2(b), two long origami sheets are attached, forming a lateral layer of a tessellation. Subsequently, multiple lateral layers are combined to create a tessellation. Theoretically, both cell-by-cell (Fig. 2(a)) and layer-by-layer (Fig. 2(b)) construction techniques can yield a tessellation with the same configuration (Fig. 2(c)). However, these two configurations will differ in terms of the materials consumed. For example, all interfacial walls in cell-by-cell construction would require double layers, while only horizontal walls will be double-layered in the layer-by-layer construction. We will account for such geometrical features when we analyze the TMP tessellations mathematically in Section 2.2.

2.1.3. Manufacturing of a TMP tessellation

Building upon the previously mentioned layer-based fabrication of a TMP tessellation, we propose an efficient manufacturing method for constructing a tessellation using polyethylene terephthalate (PET) sheets. PET sheets maintain crease lines effectively and exhibit greater resistance to moisture and fatigue effects compared to paper. Fig. 3(a) displays a sample origami sheet employed to construct a TMP tessellation. The PET sheets are cut using a laser cutting machine (Universal

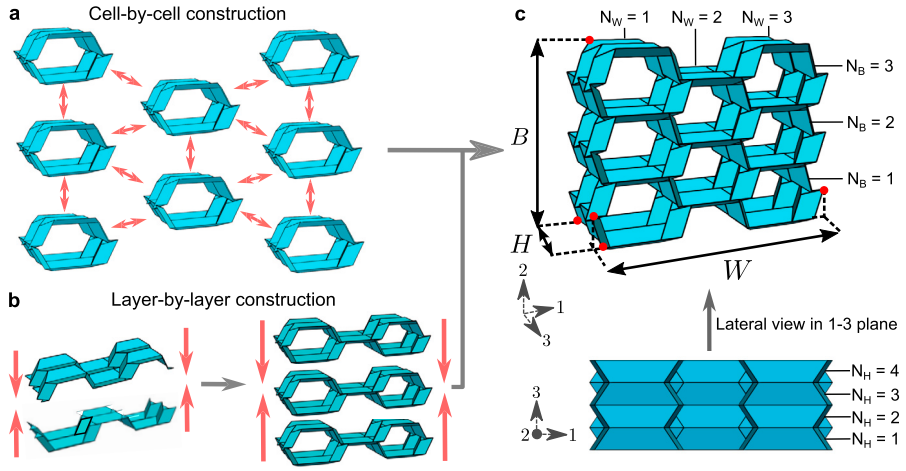

Fig. 2. A tessellation of Tachi-Miura Polyhedron. **a**, a schematic illustration of a cell-by-cell construction of a TMP tessellation. **b**, a schematic illustration of a layer-by-layer construction of a TMP tessellation. **c**, a TMP tessellation. Dimensions B, W, and H correspond to the width, breadth, and height of the structure, respectively. Also, axis numbers 1, 2, and 3 have the same direction as width, breadth, and height, respectively. N_B and N_W represent the number of unit cells in the direction of breadth and width, respectively. The inset of **c** shows the lateral view of the tessellation in the 1-3 plane. N_H represents the number of layers of the tessellation in 3-direction.

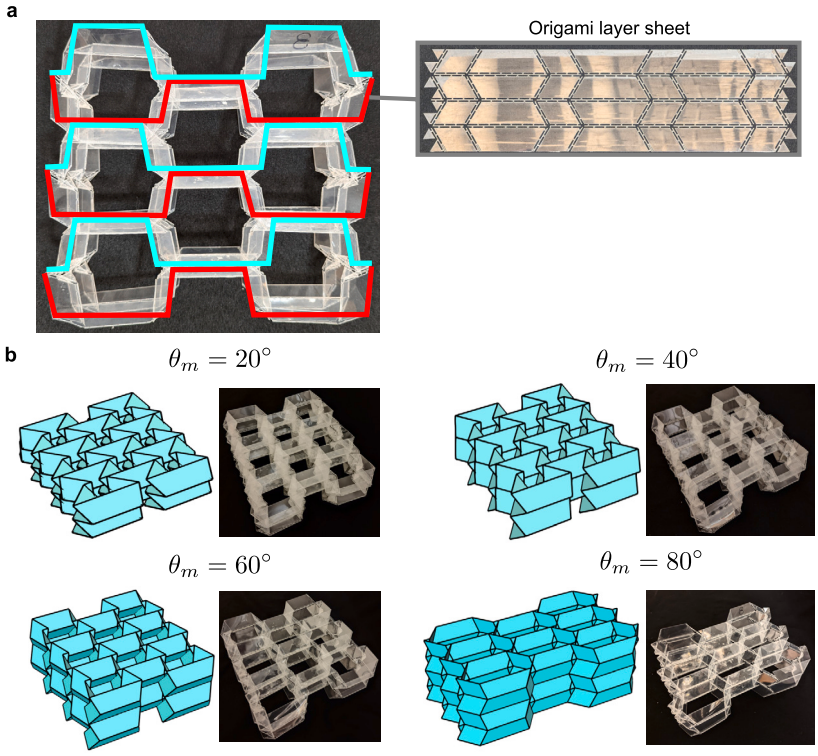

Fig. 3. Manufactured prototype of a TMP tessellation. **a**, a TMP tessellation made of six PET sheets. Red and blue lines represent the PET sheets bent downwards and upwards, respectively. The inset of **a** shows a PET origami sheet manufactured by a laser cutter. **b**, the folding process of a TMP tessellation. Each picture corresponds to a set of images of a 3D rendering and a manufactured sample with folding angles $\theta_m = 20°$, $\theta_m = 40°$, $\theta_m = 60°$, and $\theta_m = 80°$ from top left to bottom right, respectively. The folding process is also shown in the animation in Supplementary Video 1.

Laser Systems) and assembled with instant adhesive (Loctite 431). As a result of the manufacturing process discussed in the prior section, Fig. 3(a) presents a TMP tessellation comprising six origami sheets. These long sheets form a tessellation containing eight unit cells.

In Fig. 3(a), red and blue lines represent PET sheets bent downwards and upwards, respectively. As noted earlier, the horizontal facets in the tessellation exhibit double wall thickness due to PET sheet attachment, while the slanted ones maintain a single thickness of the material. Such a variation in the wall thickness implies the difference in the torsional stiffness of the creases. The mathematical model developed in Section 2.3 accounts for such TMP tessellation configurations.

Analogous to a unit cell, a TMP tessellation also demonstrates considerable shape variation by altering the folding angle, as illustrated in Fig. 3(b). Each image in Fig. 3(b) corresponds to a specific folding angle θ_m, as labeled in each panel (see Fig. 1(b) for the definition of θ_m). The folding process is further displayed in the animation provided in Supplementary Video 1.

2.2. Kinematic modeling of TMP tessellation

2.2.1. Dimensions and Poisson's ratio of TMP tessellation

We start with the analysis of the TMP tessellation in terms of the dimensions of the structure. We expand the result of the analysis of a unit cell [22] into a space-filling tessellation as shown in Fig. 2(c), where we define the breadth (B), height (H), and width (W) of the TMP tessellation (see the red markers for the exact boundaries). The analytical expression of these dimensions is as follows (see Supplementary Note A for more details).

$$\begin{aligned} B &= 2N_B m\sin\theta_g + d\cos\theta_m \\ H &= N_H d\sin\theta_m \\ W &= \max\Bigg(N_W\left(2l-\frac{d}{\tan\alpha}\right)-2(N_W-1)m\cos\theta_g, 2N_W l \\ &\quad +(N_W+1)m\cos\theta_g+\frac{d}{\tan\alpha}\Bigg) \end{aligned} \tag{1}$$

Here, for the TMP tessellation described in this manuscript, the geometrical parameters are defined as $(l,m,d,\alpha)=(28\,\text{mm},28\,\text{mm},21\,\text{mm},60°)$. The parameter $N_H=4$ represents the number of layers in the 3-direction for the TMP structure (see Fig. 2(c)). $N_B=3$ and $N_W=3$ represent the number of unit cells in the direction of breadth or width, respectively. Here, we only consider N_W to be odd-numbered for the symmetry of the tessellation. Folding angles θ_m, θ_g are defined in Fig. 1(b), and they are $\theta_m\in[0,\pi/2]$ and $\theta_g\in[0,2\alpha]$. Based on the definition of the folding angle, the tessellation is flat-folded in the 1-3 plane when $\theta_m=\pi/2$ and in the 1-2 plane when $\theta_m=0$. Based on the analytical expressions of the dimensions above, we obtain the Poisson's ratios ν_{HB}, ν_{HW}, and ν_{BW} defined as follows.

$$\begin{aligned} \nu_{HB} &= -\frac{dB/B}{dH/H} \\ \nu_{HW} &= -\frac{dW/W}{dH/H} \\ \nu_{BW} &= -\frac{dW/W}{dB/B} \end{aligned} \tag{2}$$

2.2.2. Effective density

Based on the dimensions of the TMP tessellation, we can further obtain the properties of the tessellation. The cross-sectional area A enclosed by the tessellation is obtained as follows:

$$A = 2N_{cell}m\sin\theta_m(2l+m\cos\theta_g) \tag{3}$$

where $N_{cell}=N_BN_W-(N_W-1)/2$ represents the number of the unit cells within the tessellation (see Supplementary Note A for the details). Moreover, we define the volume V as the enclosed space by the outer wall of the tessellation.

$$V = AH \tag{4}$$

Here, to evaluate the density of the system due to the volume change of the TMP tessellation, we define the effective density ρ of the tessellation:

$$\rho = \rho_{mat}\frac{V_{mat}}{V} \tag{5}$$

where V_{mat} and ρ_{mat} are the volume and density of the material used to construct the tessellation, respectively. In this work, we use PET for the manufacturing of origami-based metamaterial, and the density of PET is $\rho_{mat}=1.38\times10^{-3}\,\text{g/mm}^3$. The volume of the material V_{mat} corresponds to the total volume of the PET sheets, and it is formulated as follows:

$$V_{mat} = N_sN_H td\left(6l+4m+\frac{d}{\tan\alpha}\right) \tag{6}$$

where $N_s=2N_B$ is the number of origami sheets used to build the TMP tessellation, and $t=0.25\,\text{mm}$ is the thickness of PET.

2.3. Force-displacement relationship of the TMP tessellation

Now we investigate the force-displacement relationship of the tessellation. Due to the rigid foldability of TMP structures, we can adopt the model of approximating the TMP tessellation with rigid panels for facets and torsional springs along the crease lines [22]. We consider the folding motion of the TMP tessellation under an axial force F_3 in the direction of height. The axial force F_3 is expressed as follows (see Supplementary Note B for details):

$$\begin{aligned} F_3 = -\frac{4}{N_H d\cos\theta_m}&\left(l_m^s f(\theta_m,\theta_{mn};k_1^s,k_2^s,k_3^s)+l_m^d f(\theta_m,\theta_{mn};k_1^d,k_2^d,k_3^d)\right. \\ &\left.+l_s\frac{\cos^3(\frac{\theta_g}{2})\sin\theta_m}{\cos\alpha\sin\theta_s}f(\theta_s,\theta_{sn};k_1^s,k_2^s,k_3^s)\right) \end{aligned} \tag{7}$$

where l_m^s and l_m^d are the lengths of the main (horizontal) crease line with single and double sheet thickness, respectively, to take overlapping sheets introduced during the fabrication into account. Length l_s is the length of sub (inclined) crease lines with single sheet thickness. The function $f(\theta,\theta_n;k_1,k_2,k_3)$ represents the nonlinear spring function defined as follows.

$$f(\theta,\theta_n;k_1,k_2,k_3) = k_1(\theta-\theta_n)+k_2(\theta-\theta_n)^2+k_3(\theta-\theta_n)^3 \tag{8}$$

Here, θ_n denotes the natural folding angle of the folding process with zero potential energy. The spring coefficients k_1^s, k_2^s, and k_3^s are for the single thickness sheets. Likewise, the spring coefficients k_1^d, k_2^d, and k_3^d are for the double thickness sheets. These spring coefficients are obtained by the bending tests on the crease lines (see Supplementary Note C for the details).

Since we evaluate the mechanical property as a whole of the tessellation, the effective stress and strain in this direction can be obtained as follows:

$$\begin{aligned} \sigma_3 &= \frac{F_3}{A} \\ \epsilon_3 &= \frac{\Delta H}{H_0} \end{aligned} \tag{9}$$

where A is the cross-sectional area defined in the previous section, H_0 is the initial height of the tessellation, and ΔH is the amount by which the height of the tessellation changes. Furthermore, we derive Young's modulus E_3 of this metamaterial.

$$E_3 = \left.\frac{d\sigma_3}{d\epsilon_3}\right|_{\epsilon_3=0} \tag{10}$$

Here, Young's modulus is evaluated as the slope at the origin of the stress-strain relationship, in other words, the stiffness right after starting the compression.

2.4. Post-fabrication tuning of a TMP tessellation and experimental process

The force-displacement relationship depends not only on the design parameters of the TMP tessellation but also on its natural posture (see Eq. (8)). This natural posture is represented by the natural folding angle θ_{mn}, which is the dihedral angle between facets measured at a zero-energy state (i.e., without external forces). Fig. 4(a) shows the same TMP tessellation, but in two different zero-energy states, which tend to show different force-displacement behavior (see Fig. 4(c)). To exploit this feature for tunability in TMP-based metamaterials, we employ a heat-processing method using a convection heat oven to modify the natural folding angle of the origami structure, as schematically depicted in Fig. 4(b). Prior research has generally proposed two directions for heat-processing techniques: active actuation of origami structures using heat-activated materials like polyvinyl chloride (PVC) films [18] and shape memory composites [29], and passive control of mechanical properties through heat annealing [30].

We extend the heat annealing method for tuning the properties of origami mechanical metamaterials. We place the sample in a convec-

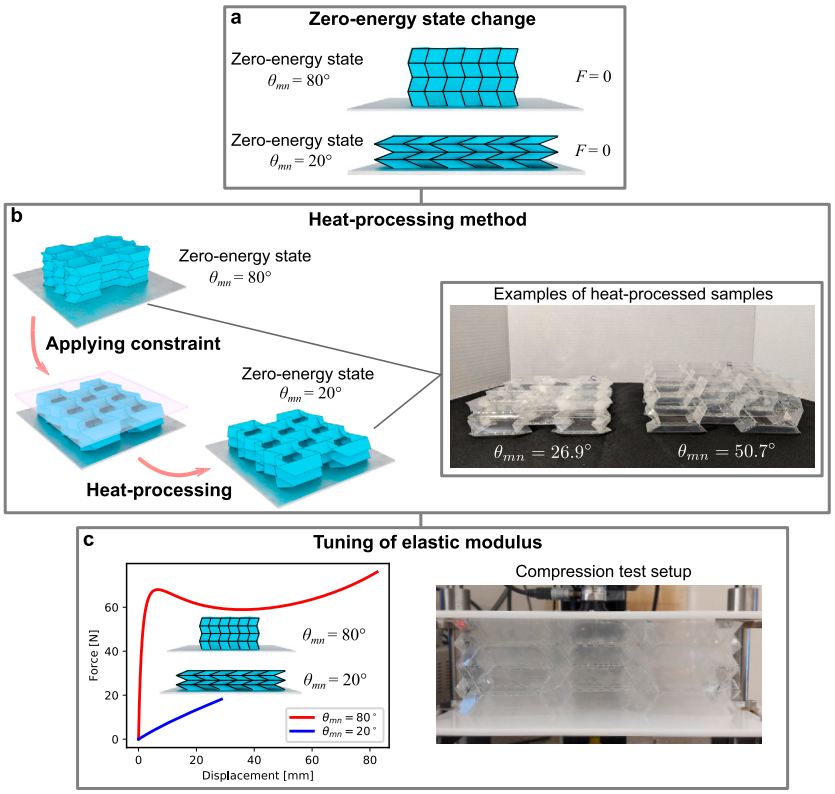

Fig. 4. Schematic figures of the post-fabrication tuning of TMP tessellation. **a**, schematic illustration of the change of the zero-energy state of TMP tessellation with two different natural folding angles. **b**, schematic illustration of the heat-processing method to change a natural folding angle of TMP structure. The inset in **b** shows two heat-processed samples with different natural postures. The left sample has a height of 38 mm ($\theta_{mn} = 26.9°$), and the right sample has a height of 65 mm ($\theta_{mn} = 50.7°$). **c**, the schematic force-displacement relationship based on the two different natural folding angles ($\theta_{mn} = 20°$ and $\theta_{mn} = 80°$). The inset in **c** shows the experimental setup to measure the force-displacement relationship and elastic modulus of the manufactured sample.

tion oven (Despatch), secure it in the desired posture, heat the structure to 80 °C for four hours, and allow it to cool to room temperature (see Supplementary Node D for the setup). Fig. 4(b) displays examples of heat-processed outcomes. The samples, manufactured with identical geometric parameters, exhibit different natural folding angles due to heat processing. Owing to the nonlinearity of the TMP tessellation's force-displacement relationship, multiple responses can be achieved from one tessellation, as illustrated in Fig. 4(c).

To investigate the broad range of Young's modulus achievable through compression tests with varying natural folding angles of the TMP tessellations, we conduct compression tests on the manufactured sample using the aforementioned tuning method. We construct an experimental setup with low-friction plates (Delrin®) and a linear stage for axial compression tests to capture the force-displacement relationship, as demonstrated in Fig. 4(c). We apply the heat process to a single fabricated sample, stage by stage, allowing us to achieve multiple natural folding angles using just one structure. For each stage, we perform a compression test to observe varying Young's modulus from one structure (see Supplementary Note E for the details).

3. Results and discussion

3.1. Kinematic analysis and effective density

First, we examine the change in dimensions as a function of the folding angle θ_m. We compress the structure using a transparent acrylic plate and measure the dimensions (see Supplementary Note F for the setup). Fig. 5(a) presents three dimensions (W, B, and H) of a TMP tessellation, revealing a significant change in dimensions between the two flat stages ($\theta_m = 0°, 90°$). Based on these dimensions, we calculate the tessellation's volume, as shown in Fig. 5(b). Similarly, by incorporating the density, we estimate the effective density of the tessellation, as demonstrated in Fig. 5(c). Both volume and density exhibit considerable changes. However, since the analysis relies on the rigid origami assumption, in which panel thickness is assumed to be zero, the analysis may be invalid when the folding angle is close to 0° or 90°. To avoid unrealistic analysis, we restrict the range of the analysis to between 20° and 80°. Within this analysis range, we find that the experimental results and the analysis are in good agreement, as illustrated in Fig. 5(a)-(c).

3.2. Poisson's ratio

We examine the Poisson's ratio of a TMP tessellation. Poisson's ratios are derived from three dimensions - height, breadth, and width - and represented as ν_{HB}, ν_{HW}, and ν_{BW} based on Eq. (2), as depicted in Fig. 6(a)-(c). Here, we present both analytical results derived from Eq. (2) and experimental measurements of the dimensions, denoted by blue solid lines and red circle symbols, respectively. Due to the non-smooth change in width measurements, we observe discontinuity in Poisson's ratios ν_{HW} and ν_{BW} (see Supplementary Notes A for details).

Poisson's ratios exhibit anisotropy in each pair of dimensions. Poisson's ratio ν_{HB} ranges from slightly negative values to highly positive values. Poisson's ratio ν_{HW} demonstrates negative values throughout the folding process. Poisson's ratio ν_{BW} displays a wide range in both negative and positive regions. Here, around $\theta_m = 50°$ in Fig. 5(a), B becomes insensitive to θ_m with showing the flat region in the graph. Therefore, dB, the infinitesimal difference of B, reaches zero. This introduces the singularity in ν_{BW} where it becomes positive or negative infinite. In the experimental verification process, we can confirm that ν_{BW} ranges from -40 to 20 with this definition of Poisson's ratio, as shown in Fig. 6(c). These findings are consistent with Poisson's ratios of TMP unit cells reported in a previous study [22]. Furthermore, they

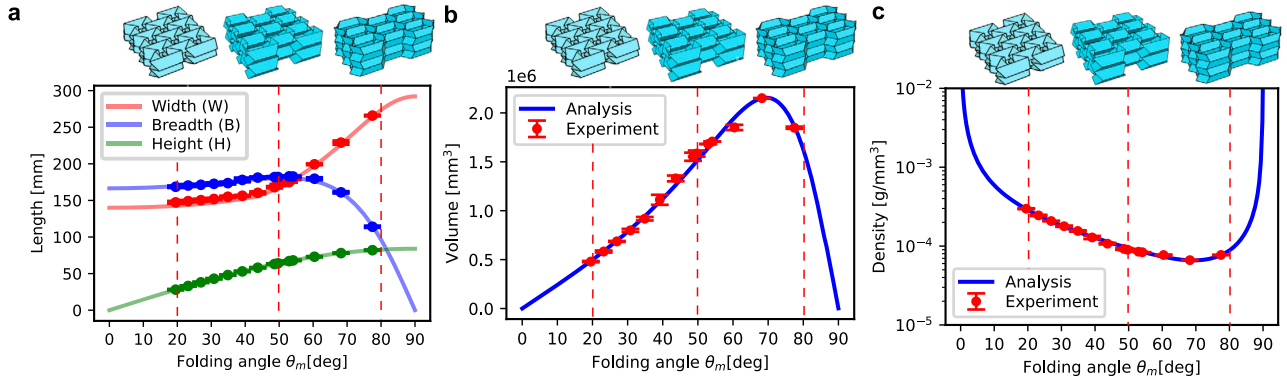

Fig. 5. Theoretical analysis and experiments on a kinematic modeling of a TMP tessellation. **a**, the three dimensions of the tessellation, W, B, and H. **b**, the volume of the tessellation. **c**, the effective density of the tessellation. Curves represent theoretical predictions based on analysis, while discrete dots and bars denote the average and standard deviation of the measurements, respectively.

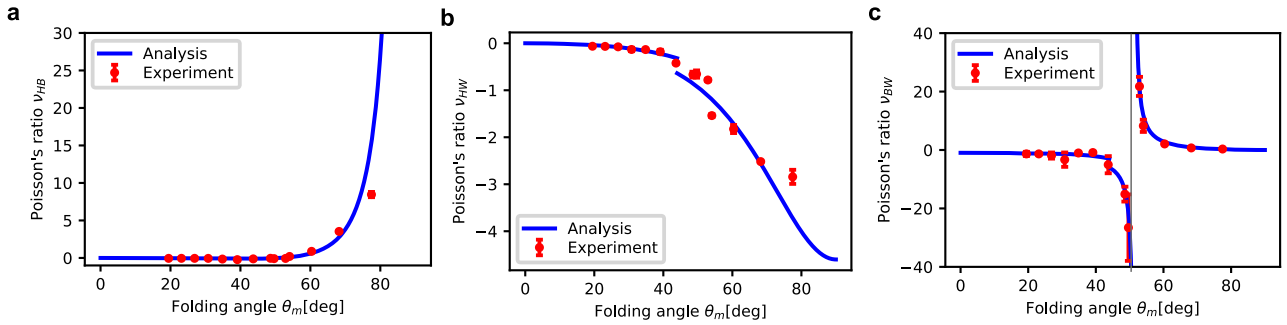

Fig. 6. Poisson's ratio of a TMP tessellation. **a**, Poisson's ratio ν_{HB}. **b**, Poisson's ratio ν_{HW}. **c**, Poisson's ratio ν_{BW}. Blue solid lines in **a** - **c** represent theoretical analysis. Red dots in **a** - **c** represent the mean values of the experiment. Red bars in **a** - **c** represent the standard deviation of the experiment. Grey vertical line in **c** represents the singular point of ν_{BW} where B becomes insensitive to θ_m (see Section 3.2 for the details).

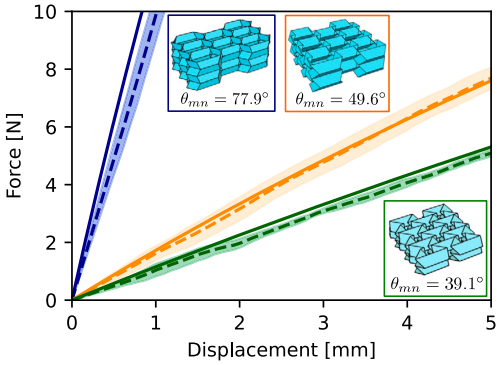

Fig. 7. Force-displacement relationship and elastic modulus of a TMP tessellation. Blue, orange, and green solid lines represent a theoretical force-displacement relationship with three different natural folding angles $\theta_{mn} = 77.9°$, $\theta_{mn} = 49.6°$, and $\theta_{mn} = 39.1°$, respectively. Dashed lines and color-shaded areas for each color depict the mean values and standard deviation of the experiments that are executed three times.

demonstrate the rich anisotropy and extensive range of Poisson's ratio, with a strong agreement between the analysis and experiment.

3.3. Elastic modulus

In this section, we examine the force-displacement relationship and Young's modulus of a TMP tessellation both theoretically and experimentally. Fig. 7 presents the theoretical and experimental force-displacement relationships for three representative natural folding angles: $\theta_{mn} = 77.9°$ ($H_0 = 82$ mm), $\theta_{mn} = 49.6°$ ($H_0 = 64$ mm), and $\theta_{mn} = 39.1°$ ($H_0 = 53$ mm). The analytical results are obtained using Eq. (7). We observe a significant difference in the force-displacement relationship depending on the natural folding angle, and the stiffness measured at the origin in Fig. 7 varies considerably with the tuning of the natural folding angle. Based on these findings, we calculate the effective stress and strain of the TMP tessellation using Eq. (9) and subsequently determine Young's modulus of the tessellation as formulated in Eq. (10). The change of Young's modulus with respect to natural folding angles is discussed in the next section. In addition to these three natural folding angles, we examine eight more natural folding angles and obtain Young's modulus for each angle (see Supplementary Note E for details).

3.4. Visualization and analysis of tunability via 3D Ashby chart

The analysis and experiments on effective density (Section 3.1), Poisson's ratio (Section 3.2), and Young's modulus (Section 3.3) yields three-dimensional Ashby charts, as shown in Fig. 8(a)-(c). The inset in Fig. 8(a) displays a two-dimensional Ashby chart with effective density and Young's modulus. This 2D Ashby chart is common in Fig. 8(a)-(c) since the only difference in Fig. 8(a)-(c) is Poisson's ratio (ν_{HB}, ν_{HW}, and ν_{BW}). These plots reveal the remarkable properties of this mechanical metamaterial, with approximately a 60-time difference in Young's modulus and a 10-time difference in density. The wide range of Young's modulus, effective density, and positive/negative anisotropic Poisson's ratio highlights the tunability of TMP origami-based mechanical metamaterials.

Moreover, we observe a unique behavior where the origami metamaterial's effective density and Young's modulus are inversely correlated, which is uncommon in traditional materials. Conventional materials tend to show stiffer behavior as their density increases. However, our TMP-based metamaterial can be designed to exhibit enhanced stiffness even under a reduced effective density. This is a highly desirable

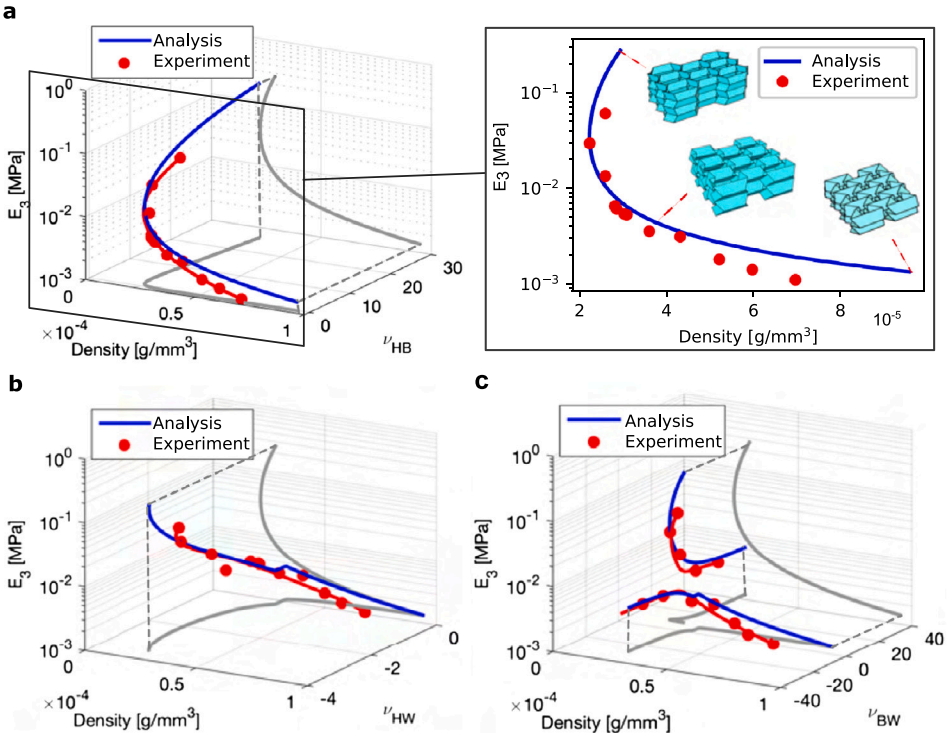

Fig. 8. Three-dimensional Ashby chart of a TMP tessellation. **a**, three-dimensional Ashby chart with effective density, Young's modulus, and Poisson's ratio ν_{HB}. The inset of **a** depicts the two-dimensional Ashby chart of effective density and Young's modulus. **b**, three-dimensional Ashby chart with effective density, Young's modulus, and Poisson's ratio ν_{HW}. **c**, three-dimensional Ashby chart with effective density, Young's modulus, and Poisson's ratio ν_{BW}. Red dots in **a** - **c** represent the mean values of the experiment. Red solid lines in **a** - **c** depict polynomial fitting to the experiment data. Gray lines in **a** - **c** represent the two-dimensional projections of the three-dimensional curves.

characteristic for constructing lightweight yet stiff structures. Remarkably, this unique property is the outcome of rigid-foldable kinematics of the TMP system, without relying on any plastic, self-locking, and/or external actuation mechanisms. The good agreement between the analysis and experiment presents the ability to predict the mechanical properties to design a tuning process to meet users' requirements.

These three-dimensional Ashby charts indicate that TMP, a 3D voluminous origami element, can serve as a building block for designing mechanical metamaterials with desired mechanical properties in terms of effective density, Young's modulus, and positive/negative anisotropic Poisson's ratio. This is achieved through a simply-fabricated single sample by applying heat processing to control the natural folding angle. The relationship between the mechanical properties behavior in a three-dimensional Ashby chart and the natural folding angle tuned by heat processing is further visualized in Supplementary Videos 2-4.

4. Conclusion

In this study, we showcase the extensive post-fabrication tunability of the TMP tessellation through theoretical analysis and experimental verification. Tailoring mechanical metamaterials after fabrication concerning three representative mechanical properties—effective density, Poisson's ratio, and Young's modulus—has been a long-standing and challenging problem. To this end, we propose and construct a prototype of an origami-based mechanical metamaterial featuring the TMP architecture. The rigid foldable nature of this TMP prototype enables an accurate prediction of these fundamental mechanical properties based on simple kinematic analysis. We employ the heat processing method to control the natural posture of the tessellation, achieving the desired properties.

The simplicity of modeling this metamaterial, assuming the structure consists of rigid panels and nonlinear torsional springs, enables us to visualize its extensive design space. We adopt the Ashby chart concept for visualization. Traditionally, the Ashby chart utilizes two material properties; however, we extend this approach to three-dimensional plots incorporating effective density, Young's modulus, and Poisson's ratio. Moreover, we experimentally verify this design space using a novel manufacturing scheme inspired by honeycomb structures. The agreement between analysis and experimentation suggests abundant opportunities to tailor these metamaterials according to users' engineering requirements. Furthermore, we observe the unique behavior of this origami-based metamaterial, where effective density decreases while Young's modulus increases.

In conclusion, the versatility of this origami-based metamaterial offers significant potential for transforming and adapting its mechanical properties to rapidly changing external environments after fabrication. TMP-based metamaterials stand out from previous research on space-filling mechanical metamaterials with lattice-based or origami-based architectures in terms of their extensive tunability, flat foldability, auxeticity, the inverse correlation between effective density and Young's modulus. Although we have explored uniform homogeneous architectures, we envision the possibility of locally tuning properties using the same units, which constitutes one of our future tasks. The dimensionless working principle of TMP metamaterial enables its application on both large scales, such as space structures and automotive airbags, and small scales, like the micro-structure of artificial bones (meta-implants [31]). Furthermore, while we consider the linear-elastic region in this manuscript, combining post-fabrication tuning, nonlinear finite element analysis, and data-driven design of metamaterials [32,33] can unlock the full potential of this metamaterial. The broad tunability of mechanical properties offers further possibilities for employing this metamaterial as a highly adaptable engineering platform.

CRediT authorship contribution statement

Koshiro Yamaguchi: Conceptualization, Investigation, Methodology, Software, Visualization, Writing – original draft. **Yasuhiro**

Miyazawa: Conceptualization, Investigation, Writing – review & editing. **Hiromi Yasuda:** Writing – review & editing. **Yuyang Song:** Conceptualization, Writing – review & editing. **Shinnosuke Shimokawa:** Conceptualization. **Umesh Gandhi:** Conceptualization, Writing – review & editing. **Jinkyu Yang:** Conceptualization, Funding acquisition, Supervision, Writing – review & editing.

Declaration of competing interest

The authors declare the following financial interests/personal relationships which may be considered as potential competing interests.

Jinkyu Yang reports financial support was provided by National Science Foundation, Toyota Research Institute North America, and National Research Foundation of Korea. Hiromi Yasuda reports financial support was provided by Japan Society for the Promotion of Science.

Data availability

Data supporting the findings of this study are available from the corresponding author on request.

Acknowledgements

We acknowledge financial support from the Toyota Research Institute North America. K.Y., Y.M., and J.Y. also thank the financial support from the U.S. National Science Foundation under Grant No. CMMI-1933729 and -2201612. J.Y. acknowledges the support from SNU-IAMD, SNU-IOER, and National Research Foundation grants funded by the Korean government [2023R1A2C2003705 and 2022H1D3A2A03096579 (Brain Pool Plus by the Ministry of Science and ICT)]. H.Y. acknowledges the support of JSPS KAKENHI Grant Number 22K18750. K.Y. is supported by Funai Foundation for Information Technology. We thank Prof. Marco Salviato and James O'Neil at the University of Washington for their assistance in the experiment process.

Appendix A. Supplementary material

Supplementary material related to this article can be found online at https://doi.org/10.1016/j.matdes.2023.112170.

References

[1] S. Babaee, N. Viard, P. Wang, N.X. Fang, K. Bertoldi, Harnessing Deformation to Switch on and off the Propagation of Sound, Adv. Mater. 28 (8) (2016) 1631–1635, https://doi.org/10.1002/adma.201504469.
[2] O.R. Bilal, A. Foehr, C. Daraio, Reprogrammable Phononic Metasurfaces, Adv. Mater. 29 (39) (2017), https://doi.org/10.1002/adma.201700628.
[3] Z. Wu, Y. Zheng, K.W. Wang, Metastable modular metastructures for on-demand reconfiguration of band structures and nonreciprocal wave propagation, Phys. Rev. E 97 (2) (aug 2018), arXiv:1709.01800, https://doi.org/10.1103/PhysRevE.97.022209.
[4] Z. Liu, X. Zhang, Y. Mao, Y.Y. Zhu, Z. Yang, C.T. Chan, P. Sheng, Locally resonant sonic materials, Science 289 (5485) (2000) 1734–1736, https://doi.org/10.1126/science.289.5485.1734.
[5] T. Frenzel, J. David Brehm, T. Bückmann, R. Schittny, M. Kadic, M. Wegener, Three-dimensional labyrinthine acoustic metamaterials, Appl. Phys. Lett. 103 (6) (2013) 61907, https://doi.org/10.1063/1.4817934.
[6] X. Zheng, H. Lee, T.H. Weisgraber, M. Shusteff, J. DeOtte, E.B. Duoss, J.D. Kuntz, M.M. Biener, Q. Ge, J.A. Jackson, S.O. Kucheyev, N.X. Fang, C.M. Spadaccini, Ultralight, ultrastiff mechanical metamaterials, Science 344 (6190) (2014) 1373–1377.
[7] K. Bertoldi, V. Vitelli, J. Christensen, M.V. Hecke, Flexible mechanical metamaterials, Nat. Rev. Mater. 2 (10 2017), https://doi.org/10.1038/natrevmats.2017.66.
[8] T. Tachi, Introduction to structural origami, J. Int. Assoc. Shell Spat. Struct. 60 (2019) 7–18, https://doi.org/10.20898/j.iass.2019.199.004.
[9] B. Haghpanah, H. Ebrahimi, D. Mousanezhad, J. Hopkins, A. Vaziri, Programmable elastic metamaterials, Adv. Eng. Mater. 18 (2016) 643–649, https://doi.org/10.1002/adem.201500295.
[10] A. Farzaneh, N. Pawar, C.M. Portela, J.B. Hopkins, Sequential metamaterials with alternating poisson's ratios, Nat. Commun. 13 (12 2022), https://doi.org/10.1038/s41467-022-28696-9.
[11] Q. Wang, J.A. Jackson, Q. Ge, J.B. Hopkins, C.M. Spadaccini, N.X. Fang, Lightweight mechanical metamaterials with tunable negative thermal expansion, Phys. Rev. Lett. 117 (10 2016), https://doi.org/10.1103/PhysRevLett.117.175901.
[12] T. Tachi, Designing freeform origami tessellations by generalizing resch's patterns, J. Mech. Des., Trans. ASME 135 (11) (2013) 1–10, https://doi.org/10.1115/1.4025389.
[13] Y. Yu, Y. Chen, G. Paulino, Programming curvatures by unfolding of the triangular resch pattern, Int. J. Mech. Sci. 238 (2022) 107861, https://doi.org/10.1016/j.ijmecsci.2022.107861.
[14] J.L. Silverberg, A.A. Evans, L. McLeod, R.C. Hayward, T. Hull, C.D. Santangelo, I. Cohen, Using origami design principles to fold reprogrammable mechanical metamaterials, Science 345 (6197) (2014) 647–650, https://doi.org/10.1126/science.1252876.
[15] E.T. Filipov, T. Tachi, G.H. Paulino, D.A. Weitz, Origami tubes assembled into stiff, yet reconfigurable structures and metamaterials, Proc. Natl. Acad. Sci. USA 112 (40) (2015) 12321–12326, https://doi.org/10.1073/pnas.1509465112.
[16] J.T.B. Overvelde, J.C. Weaver, C. Hoberman, K. Bertoldi, Rational design of reconfigurable prismatic architected materials, Nature 541 (7637) (2017) 347–352, https://doi.org/10.1038/nature20824.
[17] D. Melancon, B. Gorissen, C.J. García-Mora, C. Hoberman, K. Bertoldi, Multistable inflatable origami structures at the metre scale, Nature 592 (7855) (2021) 545–550, https://doi.org/10.1038/s41586-021-03407-4.
[18] H. Yasuda, B. Gopalarethinam, T. Kunimine, T. Tachi, J. Yang, Origami-Based Cellular Structures with In Situ Transition between Collapsible and Load-Bearing Configurations, Adv. Eng. Mater. 21 (12) (2019) 1900562.
[19] Y. Miyazawa, H. Yasuda, H. Kim, J.H. Lynch, K. Tsujikawa, T. Kunimine, J.R. Raney, J. Yang, Heterogeneous origami-architected materials with variable stiffness, Commun. Mater. 2 (1) (2021) 1–7, https://doi.org/10.1038/s43246-021-00212-4.
[20] K. Yamaguchi, H. Yasuda, K. Tsujikawa, T. Kunimine, J. Yang, Graph-theoretic estimation of reconfigurability in origami-based metamaterials, Mater. Des. 213 (2021) 110343, https://doi.org/10.1016/j.matdes.2021.110343.
[21] S. Tomita, K. Shimanuki, H. Nishigaki, S. Oyama, T. Sasagawa, D. Murai, K. Umemoto, Origami-inspired metamaterials with switchable energy absorption based on bifurcated motions of a tachi-miura polyhedron, Mater. Des. 225 (1 2023), https://doi.org/10.1016/j.matdes.2022.111497.
[22] H. Yasuda, J. Yang, Reentrant Origami-Based Metamaterials with Negative Poisson's Ratio and Bistability, Phys. Rev. Lett. 114 (18) (2015) 185502.
[23] T. Tachi, K. Miura, Rigid-foldable cylinders and cells, J. Int. Assoc. Shell Spat. Struct. 53 (174) (2012) 217–226.
[24] D. Misseroni, P.P. Pratapa, K. Liu, G.H. Paulino, Experimental realization of tunable Poisson's ratio in deployable origami metamaterials, Extrem. Mech. Lett. 53 (2022) 101685, https://doi.org/10.1016/j.eml.2022.101685.
[25] M.F. Ashby, Materials Selection in Mechanical Design, Elsevier Science, 2016.
[26] B. Han, K. Qin, B. Yu, B. Wang, Q. Zhang, T.J. Lu, Honeycomb-corrugation hybrid as a novel sandwich core for significantly enhanced compressive performance, Mater. Des. 93 (2016) 271–282, https://doi.org/10.1016/j.matdes.2015.12.158.
[27] D. Naritomi, N. Hosoya, G. Ando, S. Maeda, H. Shigemune, Creation of origami-inspired honeycomb structure using self-folding paper, Mater. Des. 223 (2022) 111146, https://doi.org/10.1016/J.MATDES.2022.111146.
[28] R. Ma, M. Li, Y. Xu, M. Meloni, J. Feng, J. Cai, Thin-Walled Structures Geometry design and in-plane compression performance of novel origami honeycomb material, Thin-Walled Struct. 181 (September) (2022) 110111, https://doi.org/10.1016/j.tws.2022.110111.
[29] M.T. Tolley, S.M. Felton, S. Miyashita, D. Aukes, D. Rus, R.J. Wood, Self-folding origami: Shape memory composites activated by uniform heating, Smart Mater. Struct. 23 (9) (2014), https://doi.org/10.1088/0964-1726/23/9/094006.
[30] B. Sargent, N. Brown, B.D. Jensen, S.P. Magleby, W.G. Pitt, L.L. Howell, Heat set creases in polyethylene terephthalate (PET) sheets to enable origami-based applications, Smart Mater. Struct. 28 (11) (2019), https://doi.org/10.1088/1361-665X/ab49df.
[31] H.M. Kolken, S. Janbaz, S.M. Leeflang, K. Lietaert, H.H. Weinans, A.A. Zadpoor, Rationally designed meta-implants: A combination of auxetic and conventional meta-biomaterials, Mater. Horiz. 5 (1) (2018) 28–35, https://doi.org/10.1039/c7mh00699c.
[32] M.A. Bessa, R. Bostanabad, Z. Liu, A. Hu, D.W. Apley, C. Brinson, W. Chen, W.K. Liu, A framework for data-driven analysis of materials under uncertainty: Countering the curse of dimensionality, Comput. Methods Appl. Mech. Eng. 320 (2017) 633–667, https://doi.org/10.1016/j.cma.2017.03.037.
[33] M.A. Bessa, P. Glowacki, M. Houlder, Bayesian machine learning in metamaterial design: Fragile becomes supercompressible, Adv. Mater. 31 (2019) 1904845, https://doi.org/10.1002/adma.201904845.